



Enhanced radiation resistance of near-infrared photoluminescence emission induced by Er/Si nanoclustering



C. Wang^a, D. Barba^{a,*}, S. Slim^a, Y.Q. Wang^c, F. Rosei^{a,b}

^a Centre Énergie Matériaux Télécommunications, Institut National de la Recherche Scientifique, Varennes, Québec J3X 1S2, Canada

^b Institute for Fundamental and Frontier Science, University of Electronic Science and Technology of China, Chengdu, PR China

^c College of Physics & The Cultivation Base for State Key Laboratory, Qingdao University, No. 308 Ningxia Road, Qingdao 266071, PR China

ARTICLE INFO

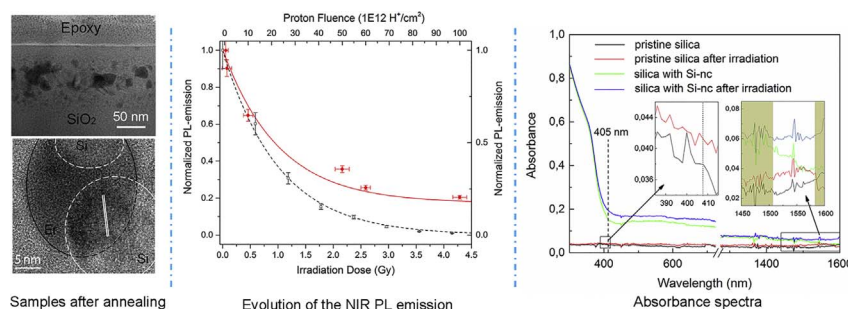
Keywords:

Erbium
Proton radiation
Transmission electron microscopy
Photoluminescence

ABSTRACT

The influence of Er and Si nanoclustering on near-infrared (NIR) Er emission is investigated in fused silica samples exposed to proton beams, used to reproduce the space radiation conditions at low-Earth orbit (LEO). Bulk silica glasses are used as model systems that mimic optical fibers. The growth of Er/Si nanoclusters, synthesized in co-implanted fused silica after thermal annealing between 1000 °C and 1200 °C, was analyzed by transmission electron microscopy (TEM) and energy-dispersive x-ray spectroscopy analysis. Photoluminescence measurements of Er³⁺ optical emission indicate that its ⁴I_{13/2} → ⁴I_{15/2} transition around 1.54 μm can still be used for optical communication after proton irradiation doses equivalent to over 50 years of exposure at LEO. Using a phenomenological model supported by Monte Carlo simulations, our results can be described in terms of an increase of the photocarrier transfer occurring between Si nanocrystals and NIR Er emitting levels, which partially compensates for the optical losses induced by structural damage. Our work demonstrates an alternative approach for the development of advanced Er light sources with superior radiation resistance and longer operating times in space environment.

GRAPHICAL ABSTRACT



1. Introduction

The vulnerability of Erbium and Ytterbium doped optical devices upon exposure to harsh environments, is an ongoing research topic for space technologies. Such devices are part of and essential to many

optical sources, gyroscopes, all fibered communication links and laser sources used in outer space [1–6]. (Er,Yb)-doped fibers are severely damaged by cosmic radiation [7,8], leading to irreversible optical losses. The space radiation environment is mainly composed (~90%) of electrons, protons and ions originating from the Van Allen belts, the sun

* Corresponding author.

E-mail addresses: barba@emt.inrs.ca (D. Barba), rosei@emt.inrs.ca (F. Rosei).

<http://dx.doi.org/10.1016/j.matdes.2017.04.016>

Received 21 December 2016; Received in revised form 4 April 2017; Accepted 5 April 2017

Available online 06 April 2017

0264-1275/ © 2017 Elsevier Ltd. All rights reserved.

and the cosmological background, as well as x-rays and gamma rays that induce similar effects in optical fibers [9,10]. Typical radiation doses associated with the proton flux at geosynchronous or low-Earth orbits (GSO/LEO) within space modules are between 80 and 120 mGy (0.8–1.2 mrad) per year [9,10]. The degradation of Er-doped fiber amplifiers (EDFAs) properties up to failure is mainly due to the generation of non-radiative trapping defects and color centers responsible for critical optical absorption in fibers of about 10 m in length [11]. Among the solutions explored to reduce the damage induced by cosmic radiation in EDFAs and improve their lifetime in space environment, H₂ loading of hermetically coated EDFAs has been proposed [12,13]. However, the formation of hydroxyl groups (OH) and sometimes hydrides (SiH) was not found to be sufficiently transparent in the near-infrared (NIR) spectral range, since its absorption peaks generate strong optical losses [14]. Other approaches based on the development of amplifiers with shorter lengths and Ce-doping were also implemented, yet these systems do not meet the requirements for satellites because they are based on the use of strong optical pumping that is too energy intensive [15].

Recently, Thomas et al. [16] suggested a solution based on the inclusion of Er-doped nanoparticles (Er-np) chemically synthesized into a nanostructured fused silica host matrix employed for the fabrication of EDFAs. Their work showed a significant improvement of the resistance to cosmic radiation in Er-np EDFAs, motivating further investigations of systems in which Er-nps and silicon-based nanoclusters coexist.

Here we studied bulk silica glass substrates as a model system that mimics optical fibers. We demonstrate that the optical emission of hybrid systems containing Er-np and silicon nanocrystals (Si-nc) is more intense and survives longer to proton radiation than the one of unmixed nanoclusterized systems. Our first step was to identify the key microstructural and phase changes in Er/Si co-implanted samples after annealing performed in the 1000 °C to 1200 °C range. We then quantified the degradation rate of the near infrared (NIR) Er-np photoemission under proton beam exposure, leading to a phenomenological description of the abnormally elevated NIR Er emission in Er/Si systems observed after irradiation tests. To this end, we conducted investigations by high-resolution transmission electron microscopy (HRTEM), followed by luminescence measurements. To simulate radiation conditions in space environment, we implemented proton irradiation experiments, supported by Monte Carlo calculations that allow us to estimate the damage rate of silicon oxide induced by impinging protons.

2. Experimental procedure

Commercial fused silica (UV-grade) substrates were initially implanted with ²⁸Si⁺ of 50 keV at a fluence of 2.0×10^{17} ions/cm², followed by Er³⁺ ions implanted at an acceleration energy of 150 keV and a fluence of 5×10^{15} ions/cm² [17–19]. These two acceleration energies were chosen to superimpose both the Si and Er depth-profiles. Annealing treatments of implanted samples were then performed inside an atmosphere controlled tubular furnace (Lindberg-Blue) for an hour, under ultra-high purity nitrogen flux (N₂) at atmospheric pressure, for annealing temperatures of 1000 °C, 1100 °C and 1200 °C.

The samples were prepared for transmission electron microscopy (TEM) imaging along their cross-section, using conventional techniques of mechanical polishing and ion thinning. The latter was carried out using the Gatan model 691 precision ion polishing system. Bright field (BF), high-angle annular dark-field (HAADF), HRTEM and energy-dispersive x-ray spectroscopy (EDS) were carried out using a JEOL JEM2100F TEM operating at 200 kV for all experiments. Photoluminescence (PL) spectroscopy measurements were conducted at room temperature using a 405 nm laser-diode excitation source, as well as an iDus InGaAs detector equipped with an ANDOR camera and a QE65000 Ocean optics detector, for measurements in the NIR and visible (VIS) ranges, respectively.

All PL measurements were recorded using the same experimental parameters and optical components. During each irradiation, a portion of the bombarded sample surface was masked by an aluminum foil to block impinging protons. The PL-signal measured in this non-damaged region was then used as reference power to quantify the variation of PL intensity after each proton beam exposure and verify that the optical alignment is unchanged. The optical absorbance measurements were carried out between 300 and 1600 nm, using a VB-400 Woollam spectrometric ellipsometer, equipped with a Xe-lamp monochromator.

The proton radiation experiments were performed inside a low-energy accelerator, equipped with a magnet mass separator and a radio frequency gas source, setting the acceleration voltage at 10 kV with the implanted area at 0.81 cm² using a collimator. According to Stopping Range of Ions in Solids and Transport of Ions in Matter (SRIM-TRIM) calculations [20], the average penetration depth of normal incident 10 keV protons into fused silica substrates is around 150 nm, with a maximum ion path of 250 nm. To simulate space conditions, the irradiation dose, *D* (in mGy), can be obtained from the proton fluence, Φ (in H⁺/cm²), by using the following equation [21]:

$$D = 1.602 \times 10^{-10} \Phi \frac{dE}{dx} \quad (1)$$

where the mass stopping power, dE/dx , (in MeV/(mg/cm²)) is equal to ~ 0.28 [20], for incident 10 keV protons into a fused silica target of mass density: $\rho = 2.30$ g/cm³.

3. Results and discussion

3.1. Microscopic investigations

BF TEM images are presented in Fig. 1a–b, and HAADF images in Fig. 1d–f, for samples annealed at 1000 °C, 1100 °C and 1200 °C, respectively. For comparison purposes, all cross sectional images were recorded at the same magnification.

In each sample, Si and Er-based nanoclusters were observed in the upper region of the implanted SiO₂ film up to a depth of 120 ± 10 nm [22]. The average dimensions of these nanoparticles were determined from an in depth analysis of TEM images, accounting for > 100 observed nanoclusters. As shown in Fig. 2, the diameter of the formed nanoclusters increases continuously with annealing temperature, from 9.9 nm at 1000 °C, to 25.0 at 1100 °C, and up to 33.0 nm at 1200 °C. Such an evolution of the nanoparticle sizes results from an Ostwald ripening mechanism and coalescence effects, as described in previous work [23,24].

HAADF analysis (also known as Z-contrast imaging) was carried out, to measure the distribution of Si and Er after annealing and show their effective overlap [24]. The thickness of the cross-sectional samples (*t*) was measured by electron energy loss spectroscopy using the Log-Ratio method [25], according to:

$$t/\lambda = \ln(I_i/I_0) \quad (2)$$

where λ is the total mean free path for inelastic electron scattering, and I_i/I_0 is the relative variation of the integrated spectral intensity with respect to the zero-loss peak. The thickness is ~ 40 nm in each sample, so that the TEM image contrast of all nanoclusters is proportional to the concentration of Er. Only incoherently scattered electrons at high angles were collected so that the acquired images can be interpreted as a result of atomic number differences inside the sample [26]. Hence, the nanoparticles with high-contrast in Fig. 1d–f can be associated with clusters containing an elevated concentration of Er. HAADF images indicate that Er atoms form larger aggregates about 33 nm in diameter at higher annealing temperatures. At 1000 °C, the depth distribution of small and isolated clusters suggests that only a small fraction of Er contributes to the formation of nanoparticles. When annealing at 1100 °C, coalescence of Er into nanoparticles is more efficient and leads to clusters richer in Er. In the sample annealed at 1200 °C, the

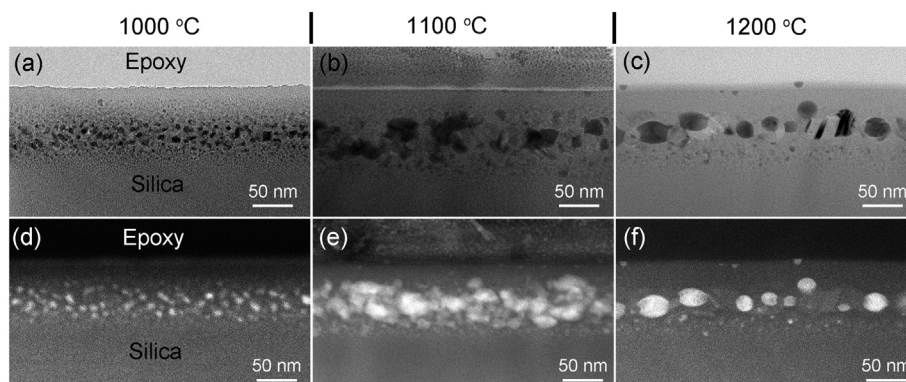


Fig. 1. BF TEM images of samples annealed at 1000 °C (a), 1100 °C (b) and 1200 °C (c); with their corresponding HAADF TEM images (d), (e) and (f).

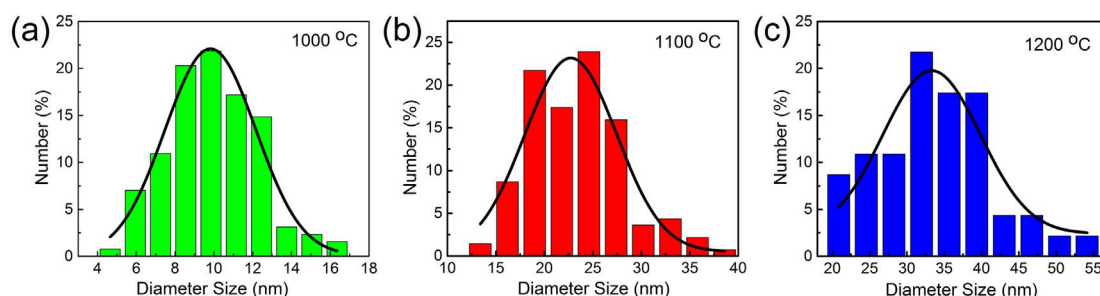


Fig. 2. Nanoparticle size-distribution of samples annealed at 1000 °C (a), 1100 °C (b) and 1200 °C (c).

observed nanoparticles were found to contain a higher concentration of Er and no other Er atoms can be observed in the surrounding SiO_2 .

The microstructure and composition of the formed nanoclusters were investigated by HRTEM. Two kinds of nanoparticles were observed in the samples annealed at 1000 °C (Fig. 3a), 1100 °C (Fig. 3b) and 1200 °C (Fig. 3c), namely: amorphous nanoparticles and atom-ordered nanocrystallites, identified by black and white circles, respectively. The inter-planar spacing (marked by a pair of parallel white lines) was measured to be 0.313 ± 0.001 nm, which corresponds to the {111} d-spacing of bulk Si.

Consequently, the white encircled nanoparticles are identified as pure Si nanocrystals (Si-nc). As for the dark amorphous nanoparticles, they were recognized as nanoclusters containing Erbium, which has a higher atomic number than Si. Since the standard molar enthalpy of Er_2O_3 formation (~ -1900 kJ/mol) is considerably lower than that of SiO_2 (~ -900 kJ/mol) and that of Erbium silicides (~ -60 kJ/mol) [27], the formation of Er_2O_3 is more favorable in the co-implanted Si/Er SiO_2 system. According to the Er–Si phase diagram [28], Er silicide precipitates can form at ~ 1210 °C. Hence, the formation of Er–O chemical bonds is strongly promoted in samples annealed at 1000 °C and 1100 °C, and the dark Erbium amorphous nanoclusters observed in Fig. 3 are most likely oxidized. Such oxidation can occur to the detriment of the Si-bond restoration inside the SiO_2 layer, where a number of broken chemical bonds have been generated during the

successive implantation of Si and Er ions [22].

HRTEM images (Fig. 4a–b) reveal the presence of stacking faults and twin boundaries inside large Si-ncs synthesized at 1200 °C. This structural defect may result from the coalescence of small Si-ncs into larger ones [17,23]. In addition, a new chemical phase (only observed at 1200 °C) was found for the nanoparticle shown in Fig. 4c–d. The inter-planar distance of its atomic structure is 0.325 ± 0.001 nm, which corresponds to the {1 $\bar{1}$ 00} inter-planar distance of hexagonal ErSi_2 [29]. Statistical analysis shows that there are approximately five times more Er_2O_3 nanoparticles than ErSi_2 nanoparticles. This demonstrates, in addition to the nucleation of pure Si-ncs, the possible formation of erbium silicide nanocrystals above 1100 °C. To test this hypothesis, EDS line scans were carried out through two different nanoparticles synthesized at 1200 °C.

An example of EDS line scan (Fig. 5a) shows that while the concentration of Si remains unchanged inside this nanoparticle, the concentrations of Er and O increase and decrease, respectively. Such features are consistent with the EDS signature of an Er-rich Si-nc, where the detected oxygen atoms mainly originate from the fused silica surroundings. On the other hand, the EDS measurements shown on Fig. 5b are compatible with a line scan of one Si-nc embedded within SiO_2 , free of Er, where the intensity peak signals of Si and O increase and decrease, correspondingly [22].

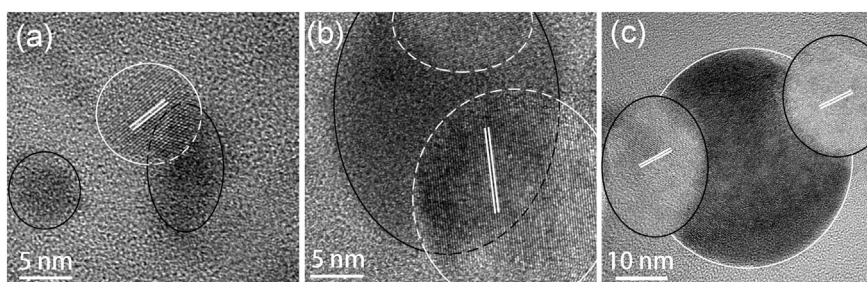


Fig. 3. HRTEM images of samples annealed at 1000 °C (a), 1100 °C (b) and 1200 °C (c), obtained at magnifications of $\times 600,000$, $\times 600,000$ and $\times 400,000$, respectively.

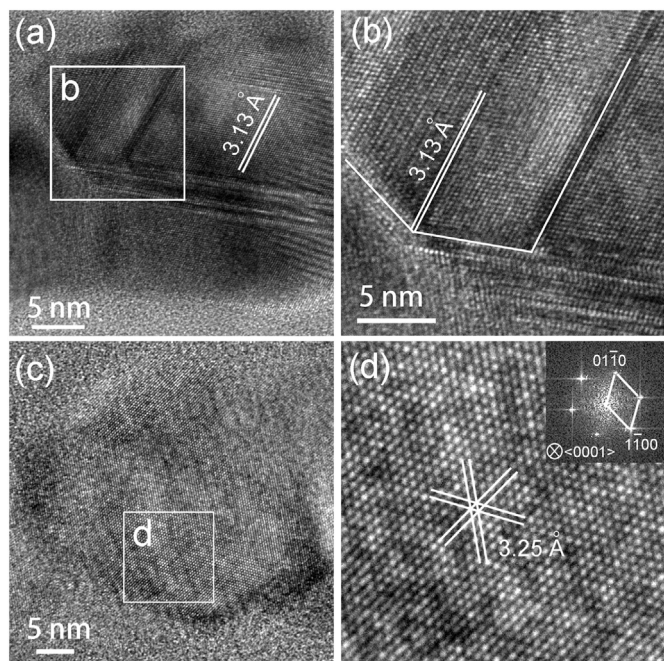


Fig. 4. (a) and (c) HRTEM images of samples annealed at 1200 °C; (b) and (d) zoomed images at a magnification of $\times 500,000$, corresponding to rectangular regions of images (a) and (c), respectively.

3.2. Photoluminescence measurements

The PL spectra of Er and Si/Er implanted samples annealed at 1000, 1100 and 1200 °C are shown in Fig. 6. No signal was detected in materials implanted exclusively with Er and annealed at 1100 °C and 1200 °C (not shown). The NIR (Fig. 6a) and VIS (Fig. 6b) emissions are associated with the $\text{Er}^{3+} - 4f: {}^4I_{13/2} \rightarrow {}^4I_{15/2}$ optical transition and the Si-nc PL, respectively [22].

In agreement with other studies on Si/Er hybrid systems [30–32], the presence of Si-ncs was found to improve the Er PL-emission around 1.54 μm . By comparing the NIR (Fig. 6a) and VIS (Fig. 6b) signals, a maximum Er PL-emission may be observed when the Si-nc PL-emission is the highest. This feature results from the occurrence of an effective transfer mechanism between the photocarriers generated by laser excitation in Si-ncs towards the NIR emitting levels of Er [33].

Fig. 6 also demonstrates that the intensity of all recorded PL signals decreases as the annealing temperature increases. The drastic reduction

of the PL peaks reported in the sample annealed at 1200 °C (Fig. 6a) has two origins: the formation of non-luminescent ErSi_2 (whose synthesis was evidenced in Fig. 4c–d) and the formation of large silicon nanoaggregates (in Fig. 4a–b). The latter observation is also consistent with the redshift of the PL peaks observed in Fig. 6b, which indicates the nucleation of large Si-ncs at higher synthesis temperatures. These clusters are made of several nanocrystallites with different atom orientations. The presence of multiple structural defects within the clusters induces strong optical absorption and/or non-radiative transitions [23].

Irradiation experiments were conducted on Si/Er co-implanted samples annealed at 1100 °C. The corresponding NIR PL spectra upon proton fluence are shown in Fig. 7a. A proton bombardment at a fluence of $1 \times 10^{12} \text{H}^+/\text{cm}^2$ was also conducted on the sample annealed at 1000 °C, which contains only Er-nps. After irradiation, the weak PL-signal reported for this sample at the bottom of Fig. 6a becomes undetectable (not shown). For samples prepared at 1100 °C, a continuous decrease of the 1.54 μm peak is reported as a function of the irradiation dose, up to 60.4 Gy, which is calculated for a proton fluence of $1.0 \times 10^{14} \text{H}^+/\text{cm}^2$ using Eq. (1). Proton fluences of 5×10^{11} , 1×10^{12} , 5×10^{12} , 1×10^{13} , 5×10^{13} , 6×10^{13} , $1 \times 10^{14} \text{H}^+/\text{cm}^2$ correspond to irradiation conditions at GSO/LEO during ~ 100 days, 200 days, 3 years, 5 years, 27 years, 32 years and 55 years, respectively [9,10]. In Fig. 7b, the normalized spectral intensity of each measured PL peak, integrated between 1480 and 1600 nm after subtracting the optical background contribution (red solid dots), is reported as a function of proton irradiation. Since the average penetration depth of 10 keV protons into SiO_2 is around 150 nm [20], most of the impinging protons have entirely crossed the layer where Si-nc and Er-np have grown (the thickness measured for the implanted sublayer is around 100 nm in Fig. 1).

Hence, the reported decrease in PL emission can be directly related to the damage generated by impinging protons, responsible for the formation of color centers that generate optical absorptions [7,34]. Typically, for Er light emission, the effect of ion bombardment or radiation exposure on PL signals should result in a single exponential decay function decreasing down to zero [35]. As evidenced in Fig. 7b, the variation in the measured PL intensities (red solid dots) does not follow this relationship. Instead, a fast reduction of the PL emission for low irradiation doses ($D < 100 \text{mGy}$) up to half the value of the non-irradiated erbium emission is observed, followed by a weak quasi-linear and continuous decrease.

The expected changes in PL intensity can be estimated on the basis of the data collected for the VIS PL signals of Si-ncs exposed to an 18 kV proton beam [35]. This extrapolation was performed with a mass

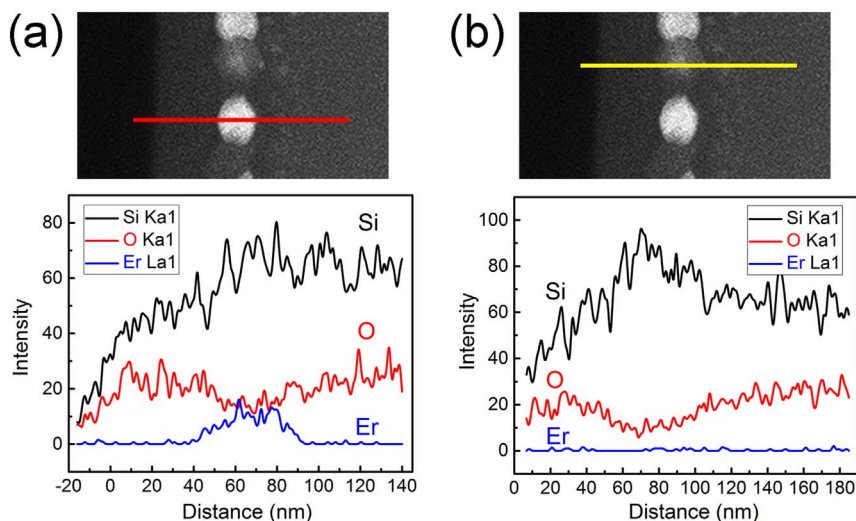


Fig. 5. EDS line-scan of bright (a) and dark (b) nanoparticles synthesized at 1200 °C, showing the neighboring formation of Er-rich Si-nc (a) and pure Si-nc (b).

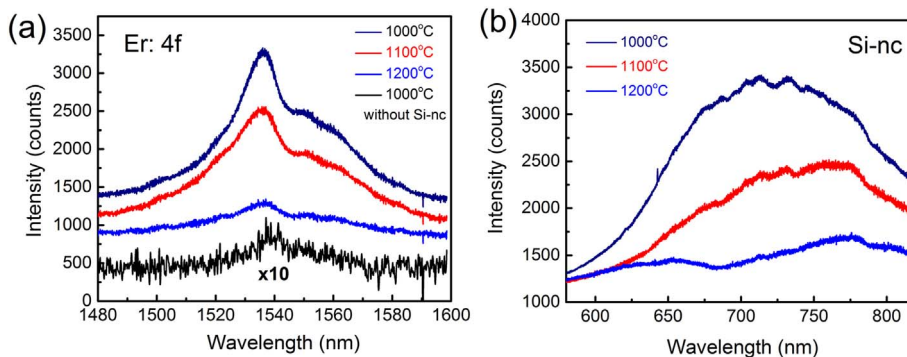


Fig. 6. PL spectra of the NIR Er emission (a) and the VIS Si emission (b).

stopping power $dE/dx = 0.37 \text{ MeV}/(\text{mg}/\text{cm}^2)$, calculated for protons accelerated at 18 kV (instead of $0.28 \text{ MeV}/(\text{mg}/\text{cm}^2)$ for 10 keV protons in this work) [35], using TRIM simulations [20]. The resulting curve (marked by black squares) indicates that ~90% of the PL signal should be lost after 2.5 Gy, while more than ~30% of the nominal Er emission is still detected (red circles). This shows that the PL-emission of erbium survives to radiation effects for longer times in Er-np/Si-nc systems.

3.3. Phenomenological analysis

Assuming that the number of emitting centers decreases according to a geometric sequence under constant particle flux bombardment, the PL-signal decay should follow a simple exponential decay function upon irradiation. Such a trend is also the one observed for the degradation of optical properties in many systems exposed to damaging radiations, such as photovoltaics cells [36] or light emitting diodes [37]. The model described and discussed below brings a new mathematical understanding to the data trend observed in Fig. 7b, to show that the PL intensity measured in Er-np/Si-nc systems does not follow the trend expected for a progressive destruction of emitting centers upon irradiation [35].

The intensity of the Er^{3+} NIR PL emission in SiO_2 , I , can be expressed as:

$$I = \tau_{PL} N_{ph}^{Er} (1 - \alpha) \quad (3)$$

where τ_{PL} refers to the erbium PL emission rate around $1.54 \mu\text{m}$, N_{ph}^{Er} to the number of $\text{Er}^{3+} : 4f$ photocarriers, and α to the fraction of PL-power absorbed by the damaged SiO_2 upper layer, which is crossed by every collected NIR photon. After exposure to a proton irradiation dose, D , this optical absorption should be proportional to the density of color

centers, assuming that the effect of OH on the upper SiO_2 matrix transparency can be neglected for low proton fluences [14]. The concentration of optical absorption centers is correlated with the concentration of recoiled target atoms, resulting from proton-matter interaction, as follows [20,38]:

$$\alpha = a \frac{n_{rec} \cdot D}{n} \quad (4)$$

where a is a dimensionless fitting parameter, related to the formation rate of color centers per recoiled atom and unit irradiation dose, n_{rec} is the density of the target atoms displaced by impinging protons, and n is the target atom density ($5 \times 10^{22} \text{ at}/\text{cm}^3$).

Using the SRIM-TRIM code [20], at depths between 20 and 80 nm, where most of Si and Er nanoclusters are formed (Fig. 1b), each incident proton moves on average 1.65×10^5 atoms along its path within the SiO_2 target. Since the volume of Erbium nanoclusters represents less than a few percent of the target volume, the damage generated inside Er-nps is negligible with respect to the damage generated by impinging protons into the host matrix. Thus, it can be postulated that the number of photocarriers generated inside emitting centers (relating to N_{ph}) and τ_{PL} remains constant during and after proton bombardment, so that the Er PL signal given in Eq. (3) should follow a single exponential decay function: $I(D) \propto \exp(-D/\Delta_1)$.

The plot (marked by dashed black lines) in Fig. 7b, showing the relative PL variations calculated for $a \sim 1/3$, supports the above mentioned mathematical trend as an accurate reproduction of the decrease in PL intensity upon proton beam exposure for irradiated Si-ncs [35]. The value of $1/3$ is consistent with the fact that 3 target atoms must be displaced to move each SiO_2 molecule, which is a prerequisite to induce a color center. From this coefficient, the calculated decay

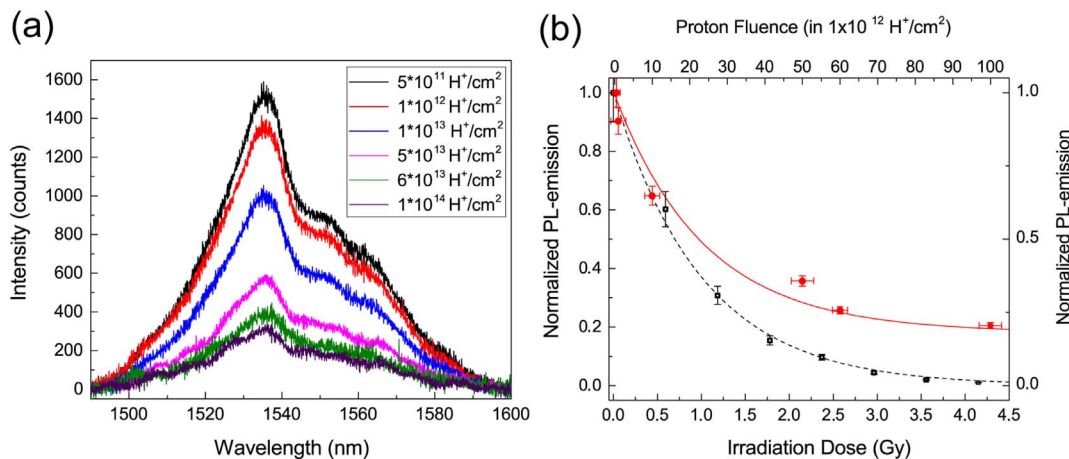


Fig. 7. Evolution of the NIR PL spectral emission of Er/Si hybrid systems synthesized at $1100 \text{ }^\circ\text{C}$ under proton irradiation (a), with the dose-dependence of their corresponding integrated signal (red solid circles) and the decay of PL power expected in single systems (black open squares) (b). (For interpretation of the references to color in this figure legend, the reader is referred to the web version of this article.)

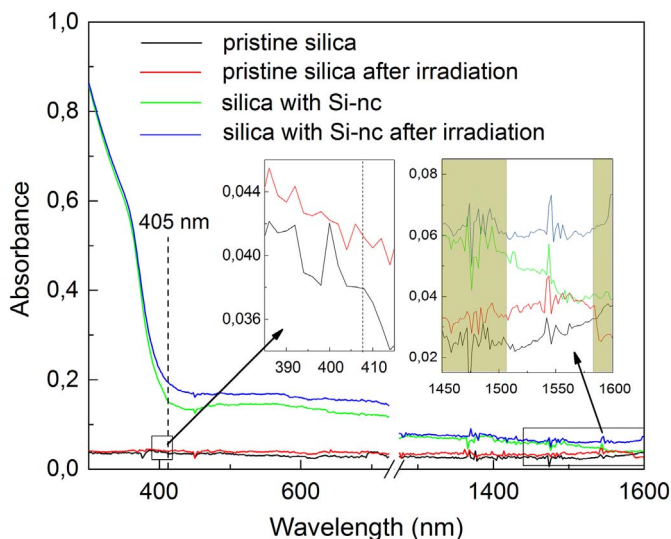


Fig. 8. Absorbance spectra measured before and after proton irradiation in pristine fused silica and fused silica where Si-ncs have been produced by 50 keV Si^+ implanted at a fluence of $2.10^{17} \text{ Si}^+/\text{cm}^2$. The insets show the variations of absorbance around the laser wavelength excitation (405 nm) and around $1.54 \mu\text{m}$ (between 1510 and 1580 nm). (For interpretation of the references to color in this figure, the reader is referred to the web version of this article.)

constant, Δ_1 , related to the evolution of the PL signal transmitted through the damaged SiO_2 layer is $\sim 1.10 \pm 0.05 \text{ Gy}$. Hence, in the absence of any charge or photocarrier transfer mechanism between emitting centers and their surroundings, this value should roughly correspond to the one of pure Er-nps embedded in SiO_2 , whose weak PL signals (Fig. 6a) become undetectable after proton irradiation experiments.

In Er-np/Si-nc systems, where the amount of $\text{Er}^{3+}:4f$ photocarriers can be improved by the occurrence of a transfer mechanism between Si-ncs and Er-np [33], the number of $\text{Er}^{3+}:4f$ photocarriers after irradiation, $N_{ph}(D)$, can be expressed as a sum of two contributions:

$$N_{ph}(D) = N_{ph}^{Er} + N_{ph}^{trans}(D) \quad (5)$$

where N_{ph}^{Er} is constant over irradiation and related to photocarriers created by optical absorption inside Er-nps, and $N_{ph}^{trans}(D)$ is the number of photocarriers generated in Si-ncs that are transferred to the NIR emitting levels of Er. Lastly, substituting N_{ph}^{Er} by $N_{ph}(D)$ in Eq. (3), the relative variation of the PL signal upon proton beam exposure can be expressed as:

$$\frac{I(D)}{I_0} \propto [1 + \beta(D)]e^{-D/\Delta_1}, \quad (6)$$

where I_0 is the PL intensity before irradiation and β refers to the effective average transfer rate of photocarriers between Si-ncs and Er-nps. By taking: $\beta \propto \exp(D/\Delta_1')$, with $\Delta_1' \sim 1.0 \text{ Gy}$, the resulting curve reported in Fig. 7b (marked in red and superimposed to red solid circles) offers a satisfactory description of the PL-signal evolution observed in irradiated Si-nc/Er-np systems. For these samples, the data obey a two exponential decay fit that can describe the evolution of the PL measurements upon irradiation only under condition $\Delta_1' < \Delta_1$. This suggests that the slower decrease of the Er signal in Er/Si hybrid systems could be explained by a greater amount of transferred photocarriers from Si-ncs towards Er following each proton irradiation. Such condition is consistent with the promotion of charge transfer mechanisms in damaged SiO_2 [35], where recoiled atoms create new electron states responsible for strong conductivity variations. Hence, due to the presence of Si-ncs, the proton-induced optical losses are compensated by a more efficient optical pumping of the NIR Er emitting centers that makes them more resistant to radiation damage effects.

Such a transfer mechanism of photo-carriers towards the emitting

$\text{Er}^{3+}:4f$ levels has been suggested by Tortech et al. [39], who related the increase of luminescence intensity reported in irradiated Er-doped optical fibers to the generation of Non-Bridging Oxygen Hole Centers (NBOHC) in the bombarded silica glass. To evaluate and compare the role of NBOHC and Si-nc in our samples, we measured the optical absorbance of pristine fused silica and fused silica substrates containing Si-ncs, before and after 10 keV proton bombardment at $10^{14} \text{ H}^+/\text{cm}^2$.

Fig. 8 shows that the changes in optical absorption due to the presence of Si-ncs are more important than those induced by proton bombardment effects. An increase by one order of magnitude is reported for the absorbance measured around 405 nm in Si-nc-based samples, with respect to the absorbance measured in pure fused silica. This suggests that the presence of Si-ncs can significantly improve the efficiency of the laser optical pumping. In fused silica samples free of Si-nc, while the increase in optical absorption at the laser excitation wavelength is marginal after irradiation ($< 10\%$, inset of Fig. 8), such an increase is $> 50\%$ in the NIR spectra range (2nd inset on Fig. 8). Such a feature means that even if the laser pumping efficiency increases after proton irradiation due to the possible creation of NBOHC or other oxygen defects by impinging protons [39], this improvement in photocarrier generation is lower than the increase of optical losses in the NIR spectral range. Hence, in the absence of Si-ncs, the Er PL-signal around $1.53 \mu\text{m}$ should decrease upon proton irradiation, as observed for Er-nps synthesized at 1000°C in pure fused silica (Fig. 6a). In samples where Si-nc has been produced, the greater impact of proton damaging effects on optical absorbance variations reported on Fig. 8 (green and blue lines) may result from a local increase of the stopping power in the Si-nc sublayer of greater mass density. For these materials, although the optical losses due to proton bombardment increase around $1.54 \mu\text{m}$, the optical absorbance is still lower in the NIR range than in the UV-VIS range. This makes thus possible the scenario proposed in our phenomenological approach, where optical losses generated by protons in NIR can be compensated by a greater generation of photo-carriers, which are transferred from Si-nc towards the $\text{Er}^{3+}:4f$ emitting levels [33]. Even if the spectra reported in Fig. 8 do not exclude a possible contribution of oxygen-related defects to the improvement of Er NIR PL-emission, they show qualitatively that such a process plays a secondary role in the studied systems.

4. Conclusions and perspectives

In conclusion, Er/Si nanoclusters synthesized in co-implanted fused silica after thermal annealing between 1000°C and 1200°C , have been studied by TEM and EDS analysis. HRTEM images showed that the diameter of the formed nanoclusters increases with temperature. At 1000°C and 1100°C , Si and Er were found to nucleate separately, leading to stronger photoemission signals in both visible and NIR spectral ranges. At 1200°C we observed nanoscale aggregates that are less optically active, due to the formation of ErSi_2 nanoclusters in localized sample regions. PL measurements of the samples exposed to proton irradiation doses equivalent to those received for > 50 years at LEO demonstrate that the intensity of the NIR Er emission around $1.54 \mu\text{m}$ decreases by only $\sim 75\%$ with respect to its nominal emission. This observation is consistent with the fact that in hybrid Er-np/Si-nc systems, the decrease of the $\text{Er}^{3+}:4f$ PL signal under proton beam does not obey a single exponential decay function upon irradiation dose, as observed for the Si-nc PL emission.

Using a phenomenological model supported by SRIM-TRIM calculations, we showed that the longer longevity of the NIR Er emission in Si-nc/Er-np samples could result from a continuous increase of the photocarrier transfer between Si-nc and Er-np. This mechanism compensates for the optical losses generated in the fused silica matrix and related to structural damaging effects induced by impinging protons. Overall, the results presented herein suggest new approaches for designing advanced Er-based components with superior performance. The integration of Si-nc inside the silica glass used for the manufactur-

ing of innovative Er-doped NIR light sources is suitable for outer space implementation, notably because both the more intense emission and the improved longevity to cosmic radiation of these systems can double or even triple their operating time.

Acknowledgements

This work was supported by the NSERC Strategic Grant STPGP 447377-13 and the MEIE PASSI 31776 Grant in partnership with MPB Technologies (Dr. Émile Haddad), as well as the NSERC Collaborative Research and Development Grant CRDPJ-461087-13 and the Prima-Québec Grant R10-006 in partnership with MPB and Plasmonique Inc. F.R. acknowledges NSERC for funding and partial salary support through an EWR Steacie Memorial Fellowship and for an individual Discovery Grant (NSERC). F.R. and D.B. are grateful to the 4th Workgroup Québec-Shandong Program [Grants nos.: 190385011 and 190385014]. Y.W. is grateful to the High-end Foreign Experts Recruitment Program [Grant nos.: GDW20163500110, GDW20143500163].

References

- [1] D. Cornwell, Space-based laser communications break threshold, *Opt. Photon. News* 5 (2016) 23–31.
- [2] J.D. Bradley, E.S. Hosseini, Monolithic erbium-and ytterbium-doped microring lasers on silicon chips, *Opt. Express* 22 (2014) 12226–12237.
- [3] J. Lee, K. Lee, Y.-S. Jang, H. Jang, S. Han, S.-H. Lee, K.-I. Kang, C.-W. Lim, Y.-J. Kim, S.-W. Kim, Testing of a femtosecond pulse laser in outer space, *Sci. Rep.* 4 (2014) 5134.
- [4] H. Chen, C. Jin, B. Huang, N.K. Fontaine, R. Ryf, K. Shang, N. Grégoire, S. Morency, R.J. Essiambre, G. Li, Y. Messaddeq, Integrated cladding-pumped multicore few-mode erbium-doped fibre amplifier for space-division-multiplexed communications, *Nat. Photonics* 10 (2016) 529–533.
- [5] E. Haddad, R.V. Kruzelecky, K. Tagziria, B. Aissa, I. McKenzie, A. Guelhan, J.-M. Muylaert, M. Celikin, D. Barba, High temperature optical fiber sensor for atmospheric reentry, Conference Paper ISCO 2016, Biarritz France, October 2016.
- [6] E. Saglamyurek, J. Jin, V.B. Verma, M.D. Shaw, F. Marsili, S.W. Nam, D. Oblak, W. Tittel, Quantum storage of entangled telecom-wavelength photons in an erbium-doped optical fibre, *Nat. Photonics* 9 (2015) 83–87.
- [7] S. Girard, B. Torteche, E. Regnier, M. Van Uffelen, A. Gusarov, Y. Ouerdane, J. Baggio, P. Paillet, V. Ferlet-Cavrois, A. Boukenter, Proton-and gamma-induced effects on erbium-doped optical fibers, *IEEE Trans. Nucl. Sci.* 54 (2007) 2426–2434.
- [8] Y. Mebrouk, F. Mady, M. Benabdesselam, J.B. Duchez, W. Blanc, Experimental evidence of Er^{3+} ion reduction in the radiation-induced degradation of erbium-doped silica fibers, *Opt. Lett.* 39 (2014) 6154–6157.
- [9] A. Holmes-Siedle, L. Adams, Handbook of Radiation Effects, Oxford University Press, New York, 1993.
- [10] R.H. Boucher, W.F. Woodward, T.S. Lomheim, R.M. Shima, D.J. Asman, K.M. Killian, J. LeGrand, G.J. Goellner, Proton-induced degradation in interferometric fiber optic gyroscopes, *Opt. Eng.* 35 (1996) 955–976.
- [11] A. Kenyon, Erbium in silicon, *Semicond. Sci. Technol.* 20 (2005) R65–R84.
- [12] K. Zotov, M. Likhachev, A. Tomashuk, M. Bubnov, M. Yashkov, A. Guryanov, S. Klyamkin, Radiation-resistant erbium-doped fiber for spacecraft applications, *IEEE Trans. Nucl. Sci.* 55 (2008) 2213–2215.
- [13] B. Brichard, A. Tomashuk, V. Bogatyryov, A.F. Fernandez, S. Klyamkin, S. Girard, F. Berghmans, Reduction of the radiation-induced absorption in hydrogenated pure silica core fibres irradiated in situ with γ -rays, *J. Non-Cryst. Solids* 353 (2007) 466–472.
- [14] O. Humbach, H. Fabian, U. Grzesik, U. Haken, W. Heitmann, Analysis of OH absorption bands in synthetic silica, *J. Non-Cryst. Solids* 203 (1996) 19–26.
- [15] A. Gusarov, M. Van Uffelen, M. Hotoleanu, H. Thienpont, F. Berghmans, Radiation sensitivity of EDFAs based on highly Er-doped fibers, *J. Lightwave Technol.* 27 (2009) 1540–1545.
- [16] J. Thomas, M. Myara, L. Troussellier, E. Burov, A. Pastouret, D. Boivin, G. Mélin, O. Gilard, M. Sotom, P. Signoret, Radiation-resistant erbium-doped-nanoparticles optical fiber for space applications, *Opt. Express* 20 (2012) 2435–2444.
- [17] M. Zhang, R. Cai, Y. Zhang, C. Wang, Y. Wang, G.G. Ross, D. Barba, Evolution of microstructural defects with strain effects in germanium nanocrystals synthesized at different annealing temperatures, *Mater. Charact.* 93 (2014) 1–9.
- [18] P. Gardner, A review of ion implantation applications to engineering materials, *Mater. Des.* 8 (1987) 210–219.
- [19] Z. Liu, M. Yang, T. Chen, Y. Liu, H.Y. Zhang, Dielectric engineering of Ge nanocrystal/ SiO_2 nanocomposite thin films with Ge ion implantation: modeling and measurement, *Mater. Des.* 83 (2015) 713–718.
- [20] J.F. Ziegler, M.D. Ziegler, J.P. Biersack, SRIM - the stopping and range of ions in matter, *Nucl. Inst. Methods Phys. Res. B* 268 (2010) 1818–1823.
- [21] A.H. Sullivan, A Guide to Radiation and Radioactivity Levels Near High Energy Particle Accelerators, Nuclear Technology Publishing, Kent, 1992.
- [22] M. Celikin, D. Barba, A. Ruediger, M. Chicoine, F. Schiettekatte, F. Rosei, Co-mediated nucleation of erbium/silicon nanoclusters in fused silica, *J. Mater. Res.* 30 (2015) 3003.
- [23] Y.Q. Wang, R. Smirani, G. Ross, F. Schiettekatte, Ordered coalescence of Si nanocrystals in SiO_2 , *Phys. Rev. B* 71 (2005) 161310.
- [24] C. Li, H. Feng, B. Liu, W. Liang, G. Liu, G.G. Ross, Y. Wang, D. Barba, Effect of nanocavities on Ge nanoclustering and out-diffusion in SiO_2 , *Nanotechnology* 28 (2017) 035707.
- [25] R.F. Egerton, Electron Energy-Loss Spectroscopy in the Electron Microscope, Springer Science & Business Media, New York, 2011.
- [26] D.B. Williams, Transmission Electron Microscopy, Springer Science & Business Media, New York, 2009.
- [27] Y.-G.F. Ren, Erbium Doped Silicon as an Optoelectronic Semiconductor Material (Doctoral dissertation), Massachusetts Institute of Technology, 1994.
- [28] S. Luzan, Y.I. Buyanov, P. Martsenyuk, Phase equilibria in the erbium-silicon system, *Powder Metall. Met. Ceram.* 36 (1997) 24–29.
- [29] A. Travlos, N. Salamouras, E. Flouda, Epitaxial erbium silicide films on (100) silicon: growth, structure and electrical properties, *Appl. Surf. Sci.* 120 (1997) 355–364.
- [30] D. Pacifici, G. Franzo, F. Priolo, F. Iacona, L. Dal Negro, Modeling and perspectives of the Si nanocrystals-Er interaction for optical amplification, *Phys. Rev. B* 67 (2003) 245301.
- [31] A. Kanjilal, L. Rebohle, M. Voelskow, W. Skorupa, M. Helm, Influence of annealing on the Er luminescence in Si-rich SiO_2 layers coimplanted with Er ions, *J. Appl. Phys.* 104 (2008) 103522.
- [32] R.A. Senter, Y. Chen, J.L. Coffey, L.R. Tessler, Synthesis of silicon nanocrystals with erbium-rich surface layers, *Nano Lett.* 1 (2001) 383–386.
- [33] D. Navarro-Urrios, O. Jambois, F. Ferrarese Lupi, P. Pellegrino, B. Garrido, A. Pitanti, N. Prtljaga, N. Daldosso, L. Pavesi, Si nanoclusters coupled to Er^{3+} ions in a SiO_2 matrix for optical amplifiers, *Opt. Mater.* 33 (2011) 1086–1090.
- [34] X. Fu, L. Song, J. Li, Radiation induced color centers in silica glasses of different OH content, *Nucl. Inst. Methods Phys. Res. B* 330 (2014) 7–10.
- [35] J. Demarche, D. Barba, G. Ross, G. Terwagne, Ionodeterioration of the silicon nanocrystal photoluminescence, *J. Appl. Phys.* 110 (2011) 114904.
- [36] Y. Yu, T. He, L. Guo, Y. Yang, L. Guo, Y. Tang, Y. Cao, Efficient visible-light photocatalytic degradation system assisted by conventional Pd catalysis, *Sci. Rep.* 5 (2015) 9561.
- [37] S.J. Pearton, F. Ren, E. Patrick, M.E. Law, A.Y. Polyakov, Review - ionizing radiation damage effects on GaN devices, *ECS J. Sol. State Sci. Tech.* 5 (2016) Q35–Q60.
- [38] J. Koutský, J. Kocik, Radiation Damage of Structural Materials, first ed., Material Science Monographs, vol. 79, Elsevier Science, 1994.
- [39] B. Torteche, S. Girard, E. Régnier, Y. Ouerdane, A. Boukenter, J.-P. Meunier, M. Van Uffelen, A. Gusarov, F. Berghmans, H. Thienpont, Core versus cladding effects of proton irradiation on erbium-doped optical fiber: micro-luminescence study, *IEEE Trans. Nucl. Sci.* 55 (2008) 2223–2228.